PPG188: Ratios of $\psi(2s)/\psi(1s)$ from Runs 14 and 15 with the FVTX

Matt Durham, Sanghoon Lim, Pat McGaughey
Los Alamos National Laboratory

April 15, 2016

1 Introduction

This Note describes the PPG188 measurement of the ratio of $\psi(2s)$ to $J/\psi(1s)$ mesons at forward rapidity, through their decays to dimuons, from the Run-14 ^{3}He+Au and Run-15 $p + p$, p+Al, p+Au data.

The analysis proceeds as follows: First, the dimuon invariant mass spectrum is prepared using tracks that are measured in the muon arms and matched to the FVTX. The fully refitted track including FVTX information is used to find the invariant mass of muon pairs. The ROOT likelihood fitter is then used to fit the invariant mass spectrum with a sum of combinatorial background, correlated background, and two peaks which represent the $\psi(1s)$ and $\psi(2s)$ charmonium states. The integrals of these peak shapes are extracted from the fit. These integrals are corrected for differences in detector acceptance and efficiency between the two states, and the ratio $\psi(2s)/\psi(1s)$ is determined. Systematic uncertainties are determined by varying the peak shapes, background normalization, and acceptance×efficiency and trigger efficiency corrections.

2 Run Selection

To ensure stable performance of the detector that is accurately modeled in simulation, runs which display unusual characteristics are not considered in this analysis. To examine the detector performance, the number of muon tracks per MB event which fire the 1D trigger is shown for each run in the Run-15 $p+p$ dataset for the North and South arms in Fig. 1. The tracks are required to satisfy nominal muon selection criteria (such last lastgap>3, etc).

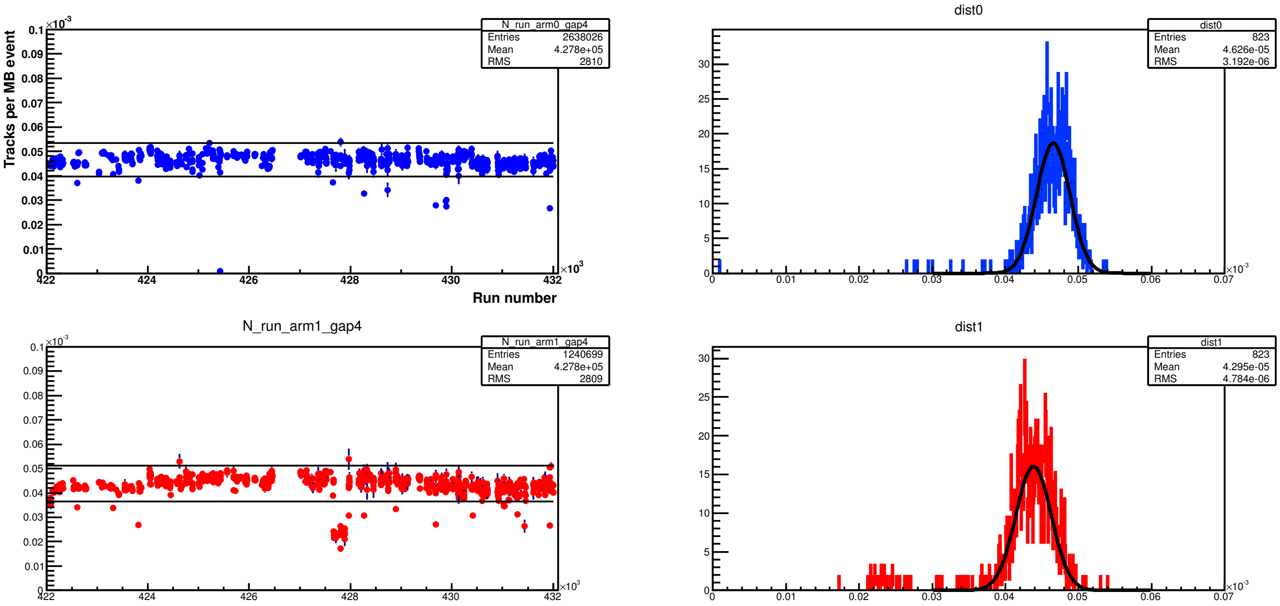

Figure 1: The number of muons per event in the South arm (blue, top row) as a function of run number (left), and the fitted distribution (right). The same plots are shown in red for the North arm in the bottom row.

A Gaussian is fit to the distribution for the North and South arms, and runs which fall outside of a window that is $\pm 3\sigma$ from the mean of the fit are discarded. Out of a total 830 runs, 12 runs are removed form consideration the South arm $p+p$ analysis, and in the North arm, 47. The width of the Gaussian fit is affected by changing detector conditions (i.e. the rate dependence of the MuID efficiencies) and the rate of double collisions. However, we note here that double collisions do not affect this analysis, as the ratio of $\psi(2s)$ to $\psi(1s)$ produced in collisions does not change.

Similar plots are shown in Fig. 2 for the p+Au data, Fig. 3 for the p+Al data, and Fig. 4 for the He+Au data.

Note there is a chunk in the middle of the p+Al data around runs 437300 to 437583 where the hit per event is lower in the South arm. This is due to problems muon tracker station 3, see Fig. 5. Rather than exclude these runs, and suffer from an undesirable loss of statistics, a separate acceptance × efficiency correction was studied for this run, see the next section for details. This loss of live area would have a large absolute correction on the yields of $\psi(2s)$, but in practice has a very small effect on the correction applied to the ratio of yields. This is due to the fact that the kinematics of dimuons from $\psi(2s)$ and $\psi(1s)$ decays are very similar, so it is difficult to affect the acceptance for one in such a way that it does not affect the other.

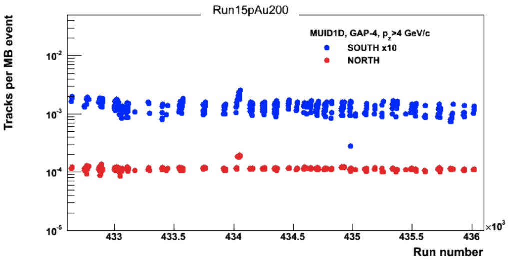

Figure 2: The number of muons per event in the South arm (blue) and North arm (red) as a function of run number for the Run-15 p+Au dataset.

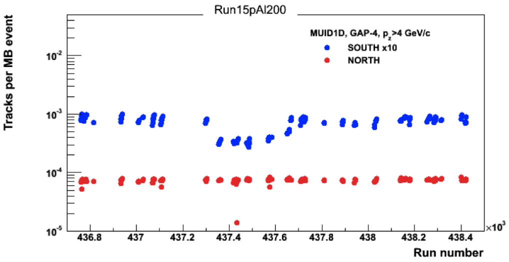

Figure 3: The number of muons per event in the South arm (blue) and North arm (red) as a function of run number for the Run-15 p+Al dataset.

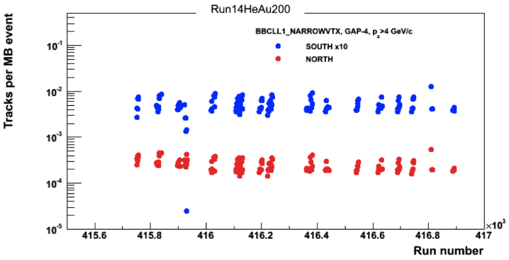

Figure 4: The number of muons per event in the South arm (blue) and North arm (red) as a function of run number for the Run-15 p+Al dataset.

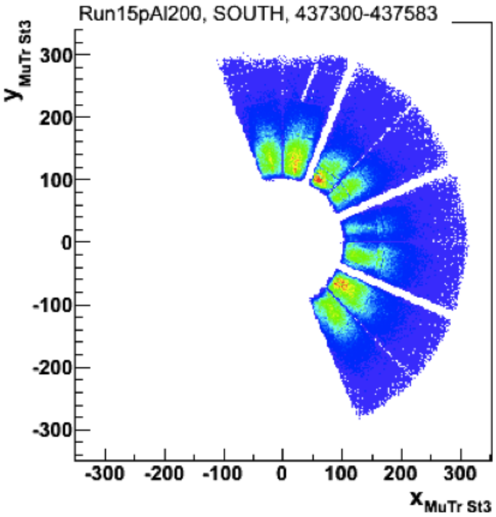

Figure 5: Stereo plot of hits in the MuTr South station 3 during the low period of the p+Al dataset.

3 Dimuon Mass

In order to extract the $\psi(2s)/\psi(1s)$ ratio, the best possible mass resolution is necessary to separate the two peaks and therefore reduce the systematic uncertainties due to overlapping tails. For this purpose, FVTX information is used as follows:

The mass of each dimuon pair is calculated using a fully refitted track that includes a MuID road with hits in the MuTracker and FVTX. Since the FVTX is located in front of the hadron absorber, the FVTX measures the muon pair opening angle before any multiple scattering in the absorber material takes place. This location, combined with the small strip size in the FVTX, gives a far superior measurement of pair opening angle (and therefore mass) than is possible with the muon tracking chambers alone.

Muon track candidates are identified using the muon arm cuts given in Tab. 1. To be considered in this analysis, tracks must reach at least the third gap in the MuID, have a good match with a MuID road, and have a reasonable chi2 value in the muon arm. Additionally, tracks that form a pair are required to pass through different octants, as typically occurs for actual charmonia dimuon decays.

Additional requirements from the FVTX further constrain the tracks and reject background, and are summarized in Tab. 2. Track matching between the FVTX and MuTr is considered in the three polar coordinates r, θ, and ϕ. As the deflection due to multiple scattering in the absorber is highly dependent on muon momentum, these cuts are sigmalized in p, and we require matching within 5σ. In addition, events are required to have a vertex position as determined by the FVTX within 40 cm of the nominal vertex position, and events are required to have fired to 2D dimuon trigger.

3.1 Combinatorial Background

Two standard methods were investigated to determine the magnitude of the uncorrelated backgrounds under the $\psi(1s)$ and $\psi(2s)$ peaks in the dimuon invariant mass spectrum: the like-sign method, which uses pairs of muons with the same charge produced in an event, and the mixed event method, which constructs pairs from muons produced in different events that have similar characteristics. Fig. 6 shows a comparison between the two methods.

Variable	Accepted Value
lastgap	>=3
DG0	$< 5\sigma$
DDG0	$< 5\sigma$
trchi2	< 23
octant cut	applied
nidhits	> 14
p_z	> 2 GeV

Table 1: Muon arm cuts (not including the FVTX).

Variable	Accepted Value
dphi_fvtx	$< 5\sigma$
dr_fvtx	$< 5\sigma$
dtheta_fvtx	$< 5\sigma$
chi2_fvtx	< 10
chi2_fvtxmutr	< 10

Table 2: FVTX cuts.

3.1.1 Like-sign Background

Using events which satisfied the same cuts used to find the unlike-sign dimuon invariant mass spectrum, the like-sign invariant mass spectrum was found for $\mu^+\mu^+$ and $\mu^-\mu^-$ pairs. The like-sign mass spectrum is normalized following the standard PHENIX methods:

$$Normalization_{ls} = \frac{2\sqrt{N_{++}N_{--}}}{N_{++}+N_{--}} \tag{1}$$

3.2 Mixed Event Backgrounds

To overcome the statistical limitations of the like-sign background subtraction methods, we use event mixing to construct a mass spectrum of muon pairs using muons produced in different events. The contributions to the spectrum are purely combinatorial, and can have no contributions from correlated dimuon emission. Following the methods used in PPG142/AN890 (where they had a similar problem with a low statistics like-sign background), the mixed events are normalized to the like-sign by the factor:

$$Normalization_{mixed} = \frac{2\sqrt{N_{++}N_{--}}}{N_{+-}^{mix}} \tag{2}$$

where N_{+-}^{mix} is the number of unlike-sign pairs from the mixed events. A curve fit to this properly normalized mixed event background is used to represent this contribution in the total fit function used to extract the peaks. A systematic uncertainty from this normalization is determined by varying the mass range over which the factor is calculated, see the section on systematic uncertainties and the related discussion for details.

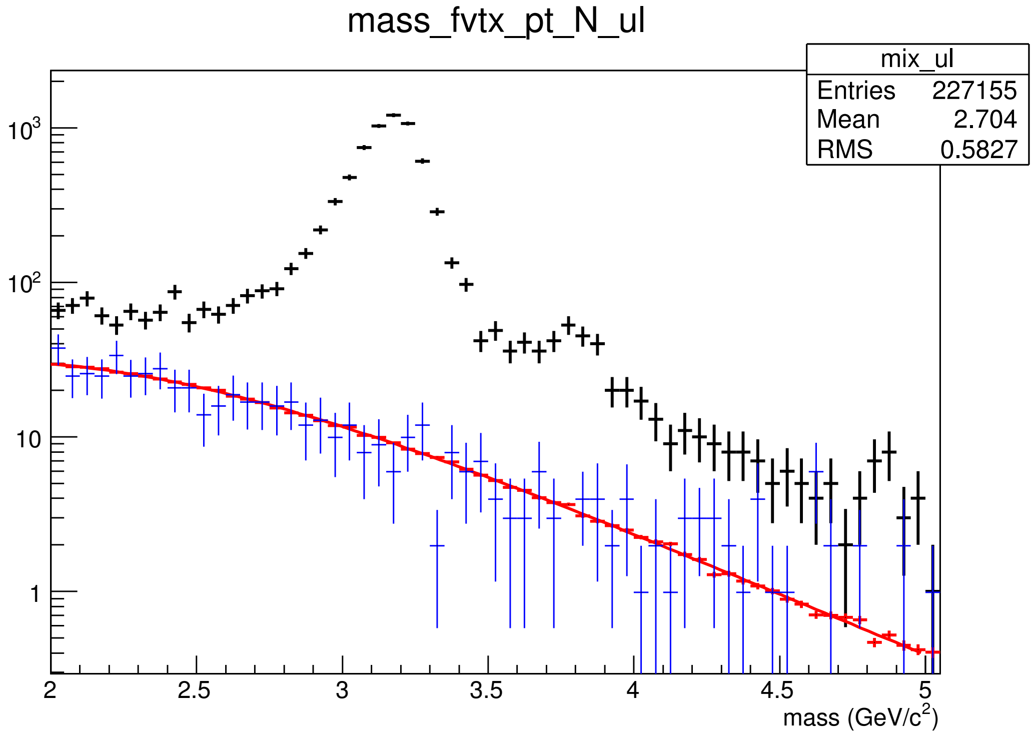

Figure 6: The unlike-sign $p + p$ dimuon mass spectra for the North arm (black), with two estimations of the combinatorial background: like-sign events are shown in blue and mixed events in red. The fit to the properly normalized mixed events is shown as the red curve.

4 Acceptance × Efficiency Corrections

The muon arm's acceptance and detection efficiency varies as a function of the muon pair's mass and momentum. Corrections to the $\psi(2s)/\psi(1s)$ ratio extracted from fits to the dimuon mass spectrum must be made in order to account for these detector effects. The acceptance and detector efficiency corrections are evaluated using PISA simulations of the PHENIX muon arms. To determine the proper corrections for both mesons, dimuon pairs over a range of mass and p_T were used as input to PISA.

The Georgia State University Dimuon Generator was used to generate 100 million dimuons with realistic properties. The rapidity, mass, and p_T distributions of the dimuons were determined by randomly sampling from representations of realistic distributions. Fig. 7 shows the distribution in rapidity of the dimuon pairs that were input to PISA. This distribution was generated by sampling from a fit to the rapidity distribution from a PYTHIA simulation of pairs which enter the muon arm solid angle. The mass distribution was found by sampling from the measured fully-corrected dimuon mass spectrum in PPG154, see Fig 9.

For each generated pair, once a mass is randomly selected from the input mass distribution, a p_T distribution is prepared for that value of mass by taking a fit to the forward $p + p$ pion spectra used in PPG153, and m_T-scaling the function to the value of the selected mass. A random value is then selected from this new m_T-scaled distribution to give the p_T value of that particular dimuon. This gives a realistic p_T distribution across the entire range of generated masses, see Fig 10.

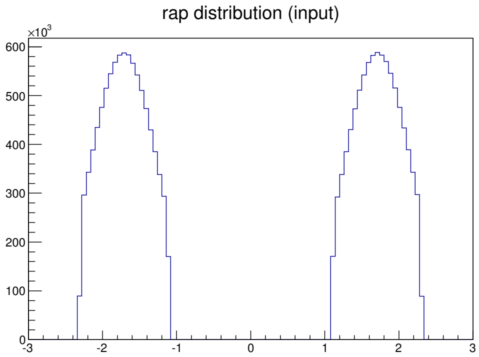

Figure 7: The rapidity distribution of the generated dimuon pairs used to determine the relative acc×eff correction factors.

These dimuons were put through the full PISA chain and reconstructed into picoDSTs. The resulting output was analyzed with identical cuts as are applied to the data. To ensure that PISA provides and accurate model of the muon arms, stereo plots of muons which pass all cuts in data and simulation are shown in Figs. 11 and 12, where good agreement is apparent. For a quantitative measure of how well the active areas match, in each arm, the distribution of all tracks in the first MuTracker station was integrated in two bins in ϕ, from -π to 0 and 0 to π. The simulation and data were normalized such that the integral in the bin from 0 to π was equal. The difference in the other bin from -π to 0 was then calculated, and is found to be 1% in the North arm and 2.4% in the South arm. In future analyses, this will be taken as a systematic uncertainty on cross sections that are determined using this simulation.

Now that were are convinced the simulated particles have realistic distributions, and that the simulation setup accurately describes the muon arms, the ratio of dimuons which satisfy all the cuts to the number of generated dimuons can be calculated to determine the acc×eff correction. This is shown in Fig. 13 along with a fit. Since we are correcting the ratio of the cross sections, the relevant correction factor is the ratios of acceptance at the $\psi(1s)$ to $\psi(2s)$ masses. These correction factors are found to be

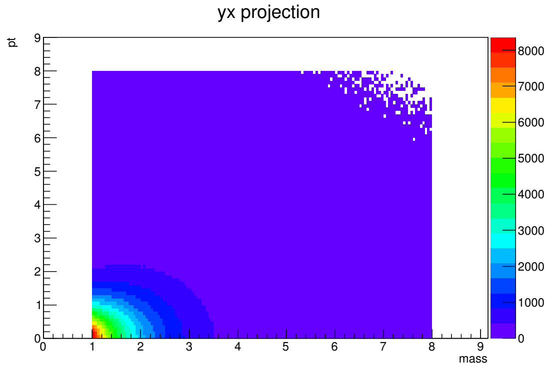

Figure 8: The mass vs p_T distribution of the generated dimuon pairs used to determine the relative acc×eff correction factors. Projections onto the mass and p_T axes are shown in Figs. 9 and 10, respectively.

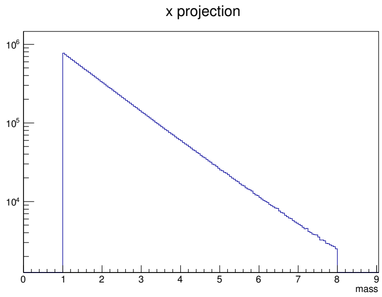

Figure 9: The mass spectrum used in the dimuon generator input to PISA. The shape is taken from the quoted measurement of the dimuon mass slope in PPG154.

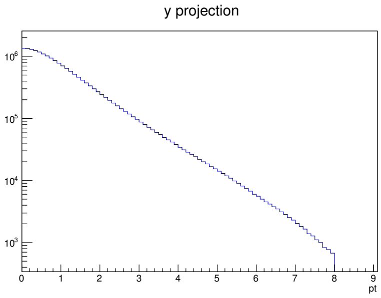

Figure 10: The p_T spectrum used in the dimuon generator input to PISA. The shape is found by fitting the forward π^0 spectrum used in PPG153 and using m_T-scaling to define a p_T spectrum to sample from at each mass.

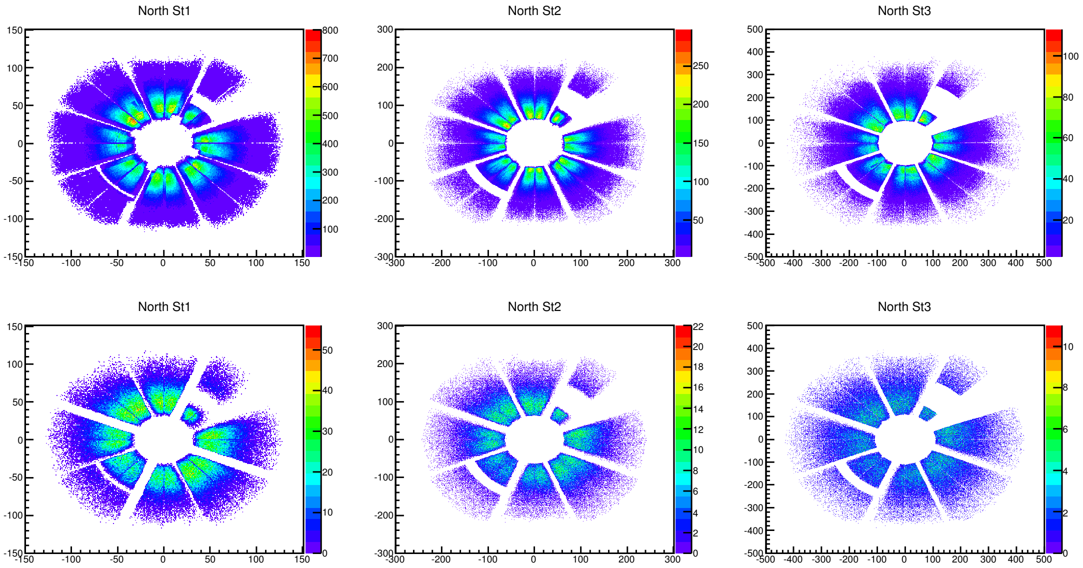

Figure 11: Stereo plots of hits from muons that pass all cuts in data (upper row) and simulation (lower row) in the three North arm muon tracker stations.

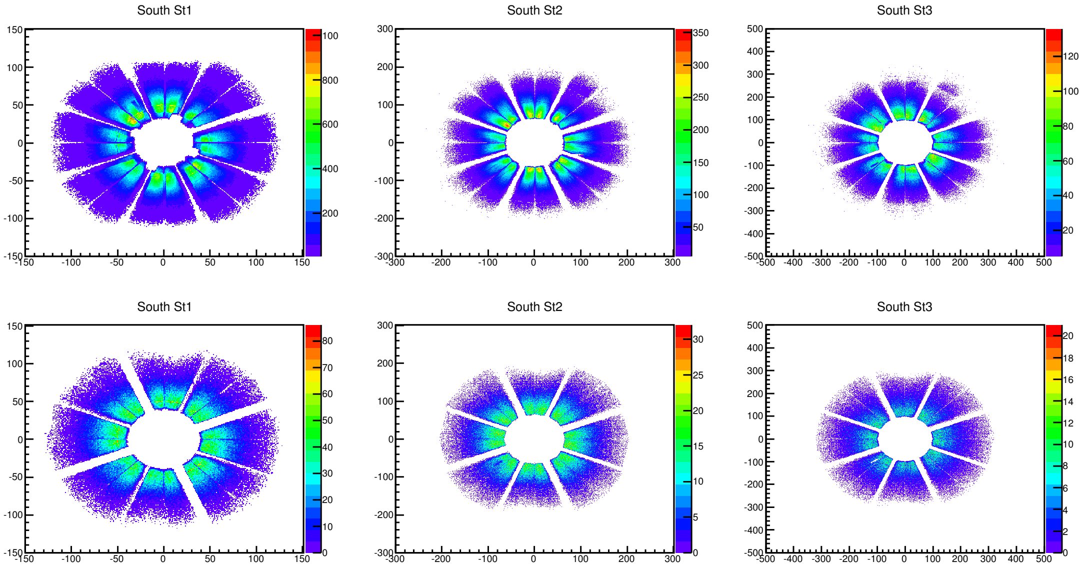

Figure 12: Stereo plots of hits from muons that pass all cuts in data (upper row) and simulation (lower row) in the three South arm muon tracker stations.

0.836 and 0.806 for the South and North arms, respectively.

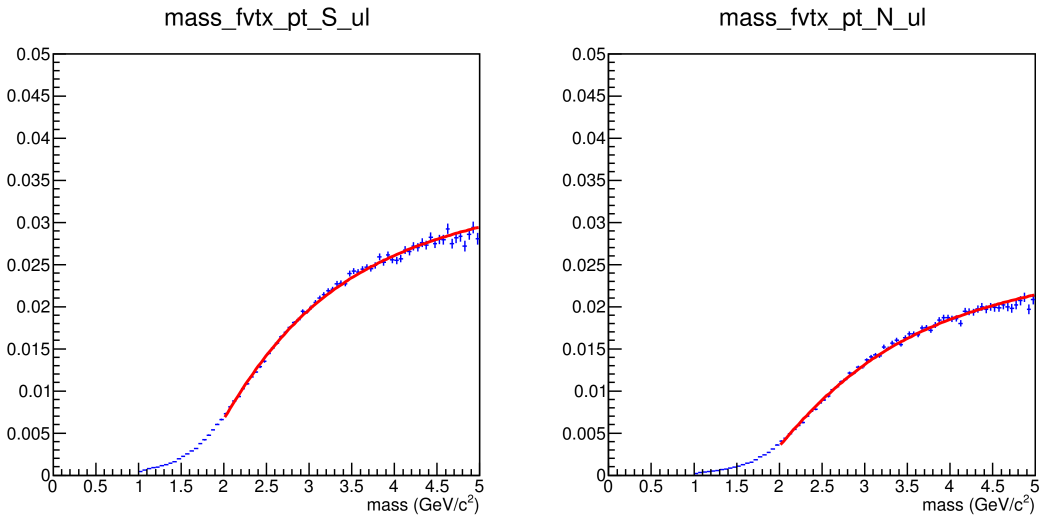

Figure 13: The curves used to find the relative acc×eff correction factors for the South (left) and North (right) muon arms. The ratios of acceptance at the $\psi(1s)$ to $\psi(2s)$ masses are 0.836 and 0.806 for the South and North arms, respectively.

There is also a subsection of runs in the p+Al dataset where half of the South MuTr station 3 was non functioning, see Fig. 5 for the data. As a check, the full acc×eff correction was re-calculated with this area masked out in simulation, see Fig. 14. The resulting curve is shown in Fig. 15. The relevant correction factor here is found to be 0.838, which, as expected, is very close to the nominal value of 0.836. This reflect the fact that the phase space for acceptance of dimuons from $\psi(2s)$ and $\psi(1s)$ is very similar, due to their similar characteristics.

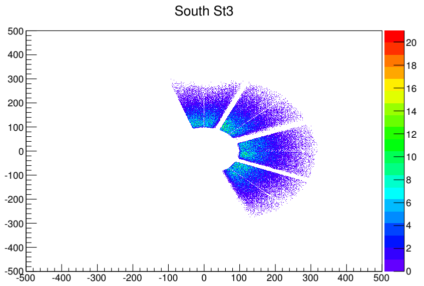

Figure 14: Stereo plot of hits in the MuTr South station 3 in the simulation examining the effect of the dead area during the subset of the p+Al dataset.

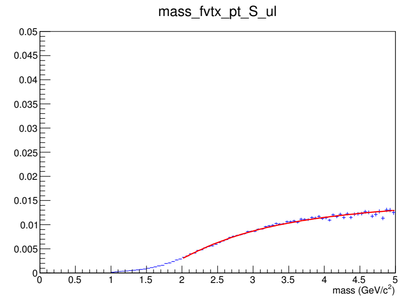

Figure 15: The curves used to find the relative acc×eff correction factors for the South (left) and North (right) muon arms. The ratio of acceptance at the $\psi(1s)$ to $\psi(2s)$ masses is 0.837.

4.1 2D Muon trigger efficiency

The 2D trigger efficiency was found as a function of mass from the Run-15 $p+p$ data set. Compared to the size of the uncertainties on the ratio, this correction is negligibly small, but we include it here for completeness.

From an analysis of the Minimum Bias data set, the trigger efficiency is the ratio of dimuons which satisfy the 2D trigger bits to all dimuons, which is shown in each arm along with a fit in Fig. 16. The relevant correction factor is the ratio of the trigger efficiency at the $\psi(1s)$ to $\psi(2s)$ masses, where the efficiency curve is quite flat. These corrections factors are found to be 0.966 and 0.969 for the South and North arms, respectively.

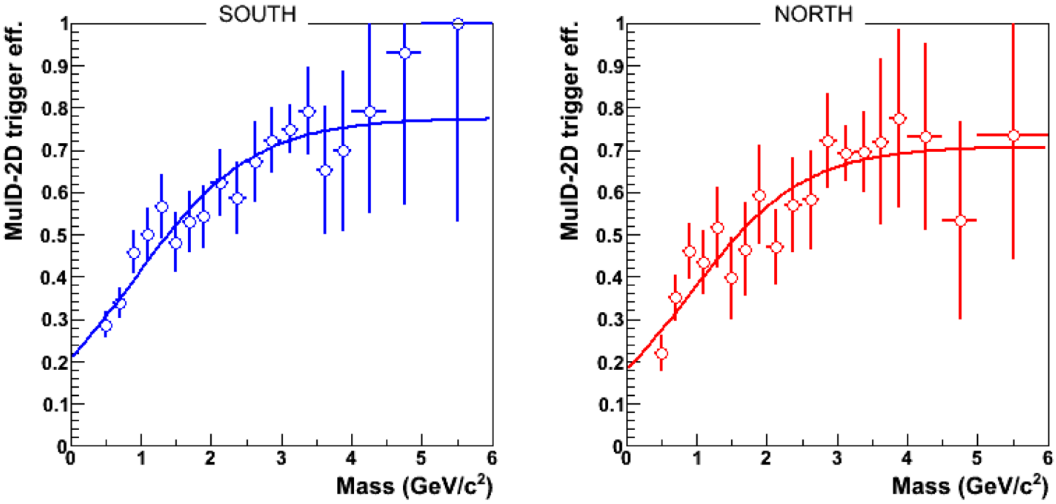

Figure 16: The curves used to find the relative trigger efficiency correction factors for the South (left) and North (right) muon arms. The ratios of efficiency at the $\psi(1s)$ to $\psi(2s)$ masses are 0.966 and 0.969 for the South and North arms, respectively.

5 Peak Extraction with the FVTX

After the dimuon mass spectrum is prepared with the cuts described previously, a fit to the raw unlike-sign counts is used to extract the peaks corresponding to the $\psi(1s)$ and $\psi(2s)$ states. The total fit function includes a fit to the properly normalized mixed event combinatorial background, an exponential function to represent the correlated background dimuons, and peaks to represent the resonances. Each of the signal peaks is represented by the sum of a Gaussian and a Crystal Ball function (which itself is a Gaussian core with a power law tail to the low side that accounts for muon pairs that are reconstructed with an erroneously low mass due to range straggling in the absorber).

The fit parameters are defined as follows:

p0 - Crystal Ball parameter α,
p1 - Crystal Ball parameter n,
p2 - $\psi(1s)$ Crystal Ball parameter μ,
p3 - $\psi(1s)$ Crystal Ball parameter σ,
p4 - $\psi(1s)$ Crystal Ball parameter N,
p5 - Gaussian parameter N,
p6 - $\psi(2s)$ Crystal Ball parameter N,
p7 - Exponential background normalization,
p8 - Exponential background slope

There are several constraints on the fit function. Since both resonance peaks are expected to display similar effects from straggling in the absorber, the Crystal Ball parameters α and n which define the low mass tail are set to be the same. The width of the $\psi(2s)$ peak is expected to be wider than the $\psi(1s)$ peak, due to the fact that the higher mass and harder p_T spectrum of the 2s state will produce higher momentum decay muons, which have a larger uncertainty in reconstructed momentum in the spectrometer. The ratio of widths of the $\psi(2s)$ to $\psi(1s)$ is set to be 1.15, according to the expected difference in mass resolution as stated in the MuTracker NIM paper. This constraint is varied to determine a systematic uncertainty (see following section and related discussion). The centroid of the $\psi(1s)$ peak is allowed to float. However, the difference between the centroids of the $\psi(2s)$ and $\psi(1s)$ peaks is set to the PDG value of 589 MeV/c^2 multiplied by the ratio of the value of the $\psi(1s)$ centroid from the fit to the PDG value of the $\psi(1s)$ mass. In practice, the difference in the fitted $\psi(1s)$ mass and the PDG value is 1-2$\%$. Changing the difference between the peaks this much makes a negligibly small change in the ratio of the two states, but should correct for any errors in the magnetic field map.

The second gaussian under each peak is set to be centered at the same mass as the Crystal Ball function. The relative normalization of the second gaussian to the Crystal Ball function is set to be the same for both resonances, since they should have the same line shape. The width of the second gaussian is set to 200 MeV in the nominal fit case, and varied to determine a systematic uncertainty (see the following section and related discussion). This is the dominant contribution to the total systematic uncertainty on the ratio.

The mass distributions for the p_T-integrated dimuon sample prepared with the cuts previously discussed are shown in Figs 17 and 18 for the Run-15 $p+p$ data in the North and South muon arms, with fits. The relevant quantities extracted from the fits are summarized in Table 3. The North and South arm $p+p$ data points are shown in Fig 19. Similar fits are shown for the other species in Figs 20 through 25.

Also of interest is the p_T dependence of the $\psi(2s)/\psi(1s)$ ratio. The mass spectra are divided into several p_T bins and the same fitting procedure is performed. Fits are shown in Figs 26 through 35 for the $p+p$ data. The other data sets do not have sufficient statistics for a meaningful p_T-dependent measurement. The ratios for the $p+p$ data are shown in p_T bins in Fig 36, which display good agreement within statistical uncertainties between the two muon arms.

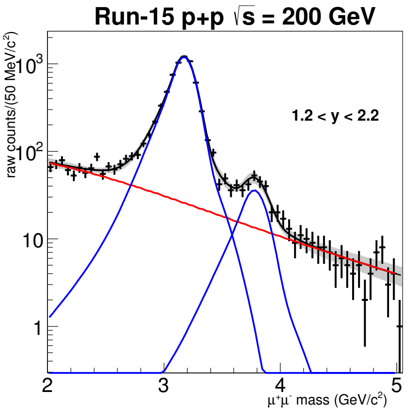

Figure 17: The unlike-sign $p + p$ dimuon mass spectra for the North arm prepared using the cuts described.

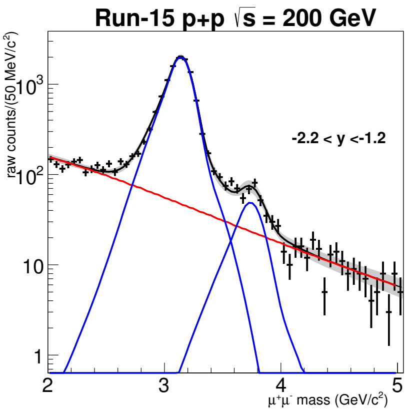

Figure 18: The unlike-sign $p + p$ dimuon mass spectra for the North arm prepared using the cuts described.

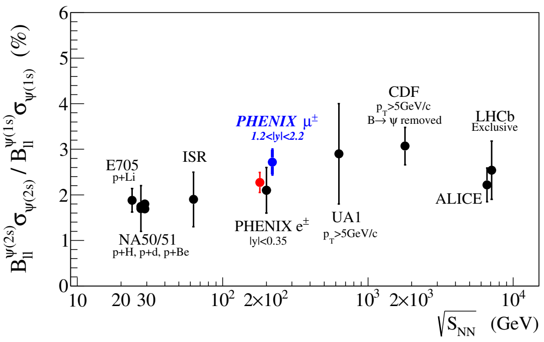

Figure 19: The ratio of inclusive $\psi(2s)/\psi(1s)$ mesons from the Run-15 $p + p$ data, for the North (blue) and South (red) arms, compared to other world data. Only statistical error bars are shown here.

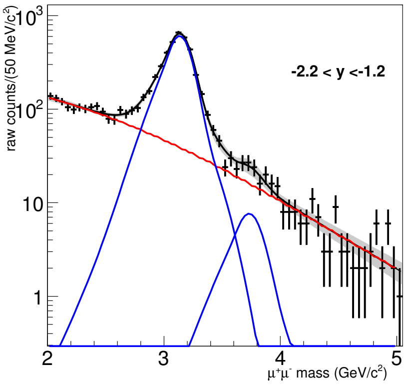

Figure 20: The unlike-sign p+Au dimuon mass spectra for the South arm prepared using the cuts described.

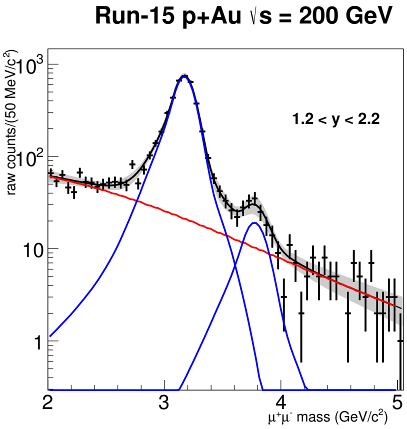

Figure 21: The unlike-sign p+Au dimuon mass spectra for the North arm prepared using the cuts described.

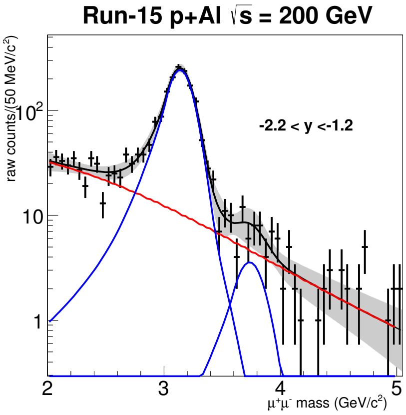

Figure 22: The unlike-sign p+Al dimuon mass spectra for the South arm prepared using the cuts described.

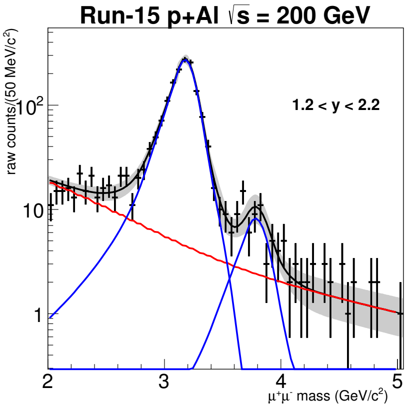

Figure 23: The unlike-sign p+Al dimuon mass spectra for the North arm prepared using the cuts described.

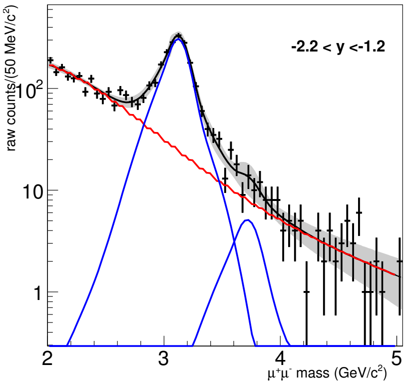

Figure 24: The unlike-sign He+Au dimuon mass spectra for the South arm prepared using the cuts described.

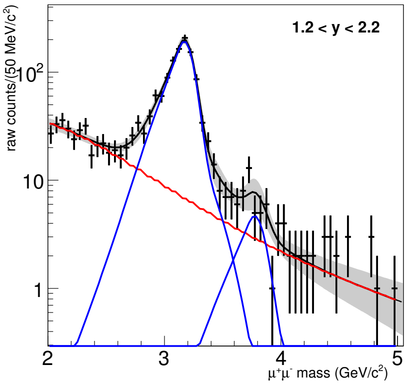

Figure 25: The unlike-sign He+Au dimuon mass spectra for the North arm prepared using the cuts described.

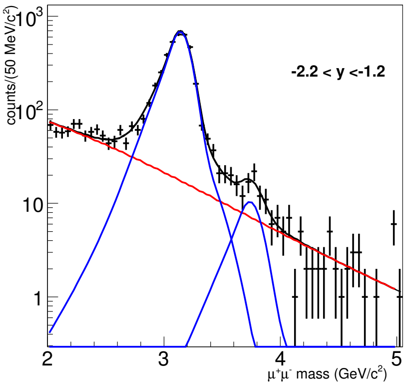

Figure 26: The unlike-sign $p + p$ dimuon mass spectra for the South arm prepared using the cuts described, in the p_T range 0-1 GeV/c.

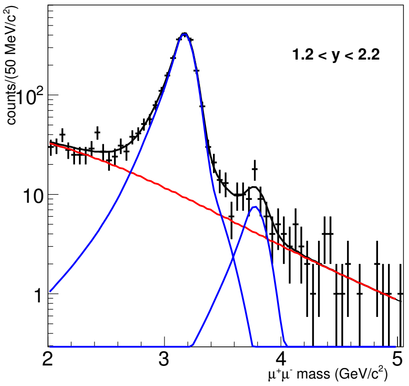

Figure 27: The unlike-sign $p + p$ dimuon mass spectra for the North arm prepared using the cuts described, in the p_T range 0-1 GeV/c.

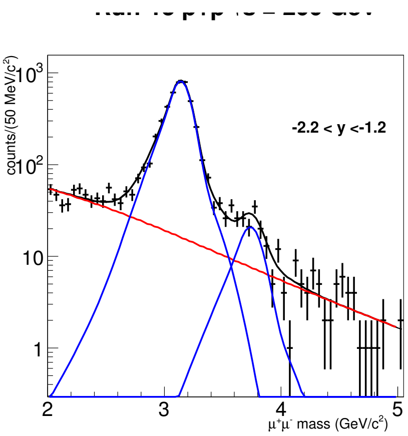

Figure 28: The unlike-sign $p + p$ dimuon mass spectra for the South arm prepared using the cuts described, in the p_T range 1-2 GeV/c.

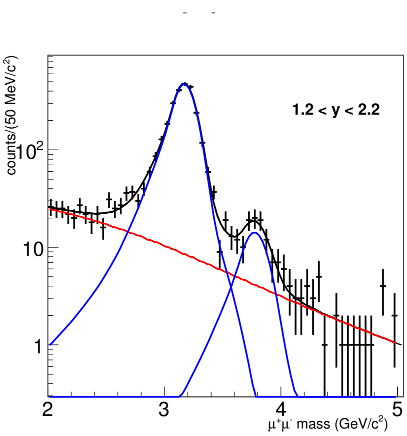

Figure 29: The unlike-sign $p + p$ dimuon mass spectra for the North arm prepared using the cuts described, in the p_T range 1-2 GeV/c.

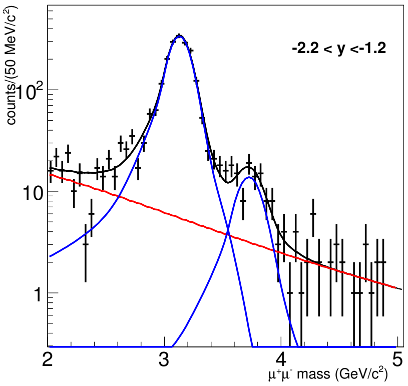

Figure 30: The unlike-sign $p + p$ dimuon mass spectra for the South arm prepared using the cuts described, in the p_T range 2-3 GeV/c.

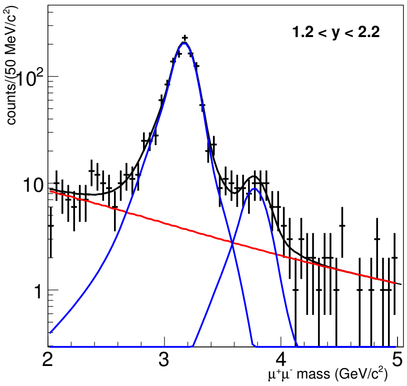

Figure 31: The unlike-sign $p + p$ dimuon mass spectra for the North arm prepared using the cuts described, in the p_T range 2-3 GeV/c.

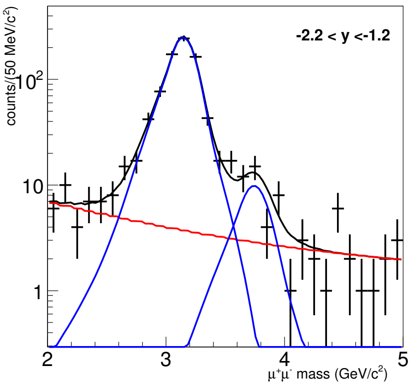

Figure 32: The unlike-sign $p + p$ dimuon mass spectra for the South arm prepared using the cuts described, in the p_T range 3-4 GeV/c.

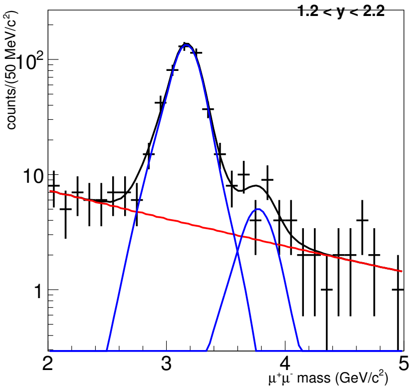

Figure 33: The unlike-sign $p + p$ dimuon mass spectra for the North arm prepared using the cuts described, in the p_T range 3-4 GeV/c.

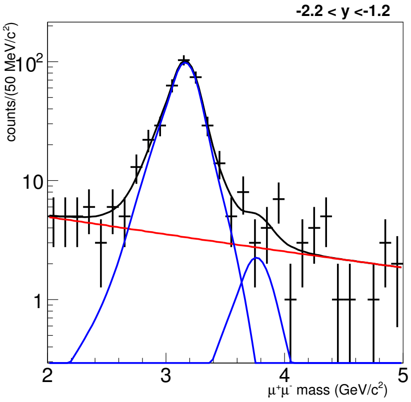

Figure 34: The unlike-sign $p + p$ dimuon mass spectra for the South arm prepared using the cuts described, in the p_T range 4-6 GeV/c.

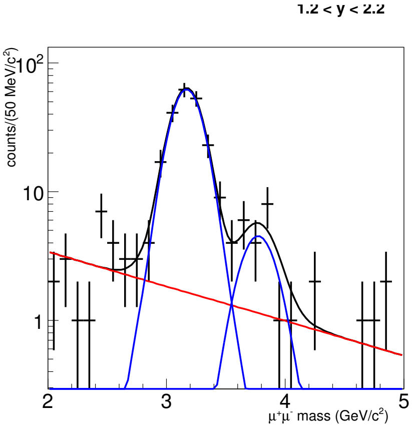

Figure 35: The unlike-sign $p + p$ dimuon mass spectra for the North arm prepared using the cuts described, in the p_T range 4-6 GeV/c.

System,Arm	$N_{\psi(1s)}$	$N_{\psi}(2s)$	Corrected $\psi(2s)/\psi(1s)$ ratio
$p+p$, N	6421±172	220±23	2.72±0.29%
$p+p$, S	10699±220	299±28	2.27±0.22%
p+Al, N	1497±142	52±11	2.73±0.64%
p+Al, S	1463±109	24.7±10.8	1.37±0.61%
p+Au, N	3893±147	117±17.8	2.38±0.37%
p+Au, S	3561±180	51±18	1.16±0.42%
^3He+Au, N	959±64	27±9.3	2.24±0.78%
^3He+Au, S	1772±132	35±14.5	1.59±0.67%

Table 3: Number of $\psi(1s), \psi(2s)$, and the corrected ratio of $\psi(2s)/\psi(1s)$, for the p_T integrated dimuon spectra for each system considered in this analysis. Note that there is good agreement on the extracted ratio between the North and South arms for the $p+p$ data, and significant differences for the other species.

System,Arm	p_T range (GeV/c)	$N_{\psi(1s)}$	$N_{\psi}(2s)$	Corrected $\psi(2s)/\psi(1s)$ ratio
$p+p$, N	0-1	2111±60	44.3±11.1	1.66±0.42%
$p+p$, S	0-1	3558±61	62±13.7	1.42±0.32%
$p+p$, N	1-2	2583±59	89.5±13.8	2.60±0.41%
$p+p$, S	1-2	4260±66	125.3±17	2.28±0.32%
$p+p$, N	2-3	1145±43	57±11.8	3.91±0.82%
$p+p$, S	2-3	1960±79	92±15.4	3.78±0.65%
$p+p$, N	3-4	417±16	18 ±7	3.64±1.45%
$p+p$, S	3-4	772±23	35±8.7	3.93±1.0%
$p+p$, N	4-6	200±30	16.6±5.3	6.54±2.30%
$p+p$, S	4-6	329±16	9±7	2.12±1.73%

Table 4: Number of $\psi(1s), \psi(2s)$, and the corrected ratio of $\psi(2s)/\psi(1s)$, in p_T bins for the Run-15 $p+p$ and $p+Au$ datasets.

6 Systematic Uncertainty Evaluation

Here the various systematic uncertainties assigned to the ratios are described. The systematic uncertainties due to the fitting procedure are determined by varying fixed parameters and re-doing the full fit to extract the ratio from the dimuon spectrum. The systematic uncertainty on the relative acc×eff correction is found by varying the assumption of the generated dimuon spectrum. The uncertainty on the relative trigger efficiency correction (which is small) is discussed. At the end of this section, and table summarizing the systematic uncertainties is given.

6.0.1 Uncertainty due to constraint on $\psi(2s)$ width

As previously described, there are several constraints on the fitting function used to determine the $\psi(2s)$ and $\psi(1s)$ yields when fitting the dimuon spectrum determined with the FVTX cuts. First we will look at the constraint on the width of the $\psi(2s)$ peak. For the central value it is constrained to be 1.15 times the width of the $\psi(1s)$ peak, due to considerations of the expected mass resolution of the muon arms as described in the NIM paper. To determine a systematic uncertainly due to this constraint, the peak width is varied down to 1.10 and up to 1.20 times the $\psi(1s)$ peak width, and the ratio is re-extracted. The results of this procedure are summarized in Table 5.

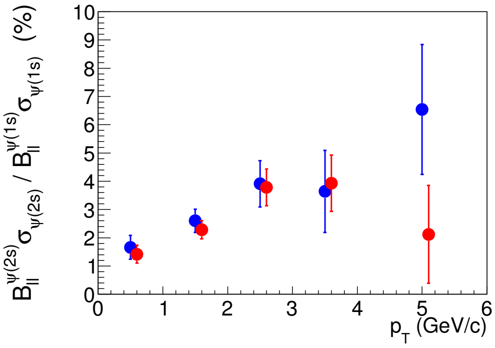

Figure 36: The ratio of inclusive $\psi(2s)/\psi(1s)$ mesons from the Run-15 $p+p$ data, for the North (blue) and South (red) arms, as a function of p_T. Only statistical error bars are shown here.

6.0.2 Uncertainty due to constraint on second Gaussian width

Another constraint on the fit is the width of the second Gaussian that is included in each peak. Previous studies have shown that this peak is likely due to tracks which are poorly reconstructed in the muon trackers. However, simply excluding all these tracks gives an undesirable loss of statistics. Selecting only these tracks gives a $\psi(1s)$ width near 200 MeV. Therefore, the width of the second Gaussian is set to 200 MeV in the fitting routine. A systematic uncertainty is determined by varying this peak width between 150 and 250 MeV and repeating the fits. A summary of the changes in the ratio due to the variation of this width is shown in Table 6.

This is the dominant systematic uncertainty on this measurement. We note that this systematic varies a bit between the different species. This is not unexpected. The systematic is quite small for $p+p$, due to the low combinatorial background. This becomes a significantly larger effect for ^3He+Au in the Au-going direction, because there the combinatorial background is significant and the $\psi(2s)$ yield is suppressed. Therefore small changes in the peak shape (and therefore background) give rise to significant changes in the integral under the $\psi(2s)$ peak.

6.0.3 Uncertainty due to mixed-event normalization range

The mass range over which the mixed-event combinatorial background is normalized to the like-sign dimuon spectrum may also affect the peak yields. In the nominal case, the mass range is 2-5 GeV. This range is varied to include the ranges 1.5-5 GeV and 2.5-5.5 GeV. The changes in the extracted ratios are summarized in Table 7.

6.0.4 Uncertainty due to relative acc × eff correction

The acceptance × efficiency correction used to find the central value of the $\psi(2s)/\psi(1s)$ ratio was calculated using a simulated dimuon spectrum with a p_T spectrum determined by m_T scaling the forward rapidity pion spectrum from 200 GeV $p+p$ collisions. To determine a systematic uncertainty, the input spectrum was modified and the effect on the correction was observed. Specifically, the p_T dependence of the nuclear modification factor of J/ψ mesons from PPG125 was fit and used to modify the generated dimuon p_T spectrum. The complete simulation chain was re-done with these three different cases of assumed p_T distributions and the correction factor, defined as the ratio of the acceptance × efficiency correction at the J/ψ mass to the acceptance × efficiency correction at the $\psi(2s)$ mass, was calculated

System,Arm	Ratio of 2s to 1s width	Corrected $\psi(2s)/\psi(1s)$ ratio	Deviation from central value
$p+p$, N	1.15 (nominal)	2.72%	N/A
$p+p$, S	1.15 (nominal)	2.27%	N/A
$p+p$, N	1.2	2.78%	2.2%
$p+p$, S	1.2	2.33%	2.6%
$p+p$, N	1.1	2.65%	2.6%
$p+p$, S	1.1	2.17%	4.4%
p+Al, N	1.15 (nominal)	2.73%	N/A
p+Al, S	1.15 (nominal)	1.37%	N/A
p+Al, N	1.2	2.81%	2.9%
p+Al, S	1.2	1.42%	3.7%
p+Al, N	1.1	2.65%	2.9%
p+Al, S	1.1	1.32%	3.6%
p+Au, N	1.15 (nominal)	2.38%	N/A
p+Au, S	1.15 (nominal)	1.16%	N/A
p+Au, N	1.2	2.41%	1.3%
p+Au, S	1.2	1.19%	2.6%
p+Au, N	1.1	2.34%	1.7%
p+Au, S	1.1	1.12%	3.4%
^{3}He+Al, N	1.15 (nominal)	2.24 %	N/A
^{3}He+Al, S	1.15 (nominal)	1.59%	N/A
^{3}He+Al, N	1.2	2.29%	2.2%
^{3}He+Al, S	1.2	1.64%	3.1%
^{3}He+Al, N	1.1	2.18%	2.7%
^{3}He+Al, S	1.1	1.53%	3.8%

Table 5: Summary of changes in the ratio of $\psi(2s)/\psi(1s)$ when adjusting the fit constraint on the width of $\psi(2s)$ peak from its central value of 1.15.

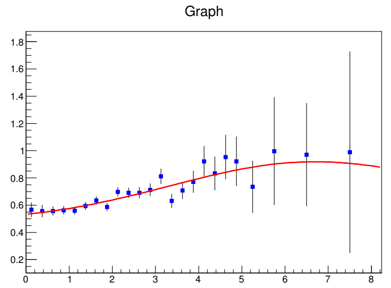

Figure 37: Fit to the most central J/ψ R_{dA} data from PPG125 at forward rapidity.

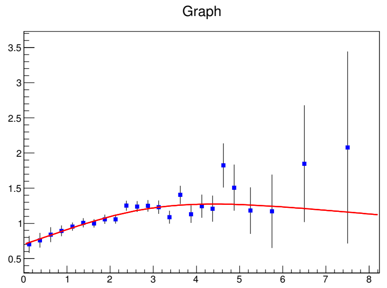

Figure 38: Fit to the most central J/ψ R_{dA} data from PPG125 at backward rapidity.

for each case and tabulated in Tab. 8. A conservative systematic uncertainty of 2% is assigned to each arm to cover the differences in the relative correction.

System,Arm	Second Gaussian width (MeV)	Corrected $\psi(2s)/\psi(1s)$ ratio	Deviation from central value
$p+p$, N	200 (nominal)	2.72%	N/A
$p+p$, S	200 (nominal)	2.27%	N/A
$p+p$, N	250	2.49%	8.5%
$p+p$, S	250	1.99%	12.3%
$p+p$, N	150	2.94%	8.1%
$p+p$, S	150	2.59%	14.1%
p+Al, N	200 (nominal)	2.73%	N/A
p+Al, S	200 (nominal)	1.37%	N/A
p+Al, N	250	2.77%	1.5%
p+Al, S	250	1.24%	9.5%
p+Al, N	150	2.76%	1.1%
p+Al, S	150	1.52%	10.9%
p+Au, N	200 (nominal)	2.38%	N/A
p+Au, S	200 (nominal)	1.16%	N/A
p+Au, N	250	2.07%	13%
p+Au, S	250	0.95%	18.1%
p+Au, N	150	2.65%	11.3%
p+Au, S	150	1.09%	6%
^{3}He+Al, N	200 (nominal)	2.24%	N/A
^{3}He+Al, S	200 (nominal)	1.59%	N/A
^{3}He+Al, N	250	1.90%	14.7%
^{3}He+Al, S	250	1.04%	34.6%
^{3}He+Al, N	150	2.52%	12.5%
^{3}He+Al, S	150	2.23%	40.2%

Table 6: Summary of changes in the ratio of $\psi(2s)/\psi(1s)$ when adjusting the fit constraint on the width of the second Gaussian peak from its central value of 200 MeV.

6.0.5 Uncertainty due to relative trigger efficiency

The correction applied to the $\psi(2s)/\psi(1s)$ ratio to account for the difference in 2D dimuon trigger efficiency at the different masses is 0.969 in the North arm and 0.966 in the South arm. We take a conservative estimate of 25% as the uncertainty on this correction factor, and round that up to a relative uncertainty of 1% on the ratio for each arm.

A summary of all systematic uncertainties on the ratio $\psi(2s)/\psi(1s)$ is given in Table 9 for the $p+p$ data, and Tabs. 10 through 12 for the p+Al, p+Au, and He+Au data. For the fitting uncertainties (where parameters are varied up and down), the final systematic uncertainty is found by averaging together the effect found by the upward and downward variations. All the systematics are added in quadrature to give the total systematic uncertainty for each arm.

Since the $p+p$ system is symmetric, the ratios from the North and South arm a combined via a weighted average to produce one number for the $\psi(2s)/\psi(1s)$ ratio at forward rapidity, following the procedure in the PDG. The combined systematic uncertainty is found by averaging the systematic uncertainties of each arm, weighted by the statistical uncertainty on that arm. The final value is 2.43 ± 0.18 (stat) ± 0.29 (sys) %.

System,Arm	Mass range for normalization (GeV)	Corrected $\psi(2s)/\psi(1s)$ ratio	Deviation from central value
$p+p$, N	2-5 (nominal)	2.72%	N/A
$p+p$, S	2-5 (nominal)	2.27%	N/A
$p+p$, N	1.5-5	2.72%	0.0%
$p+p$, S	1.5-5	2.28%	0.4%
$p+p$, N	2.5-5.5	2.72%	0%
$p+p$, S	2.5-5.5	2.27%	0%
p+Al, N	2-5 (nominal)	2.73%	N/A
p+Al, S	2-5 (nominal)	1.37%	N/A
p+Al, N	1.5-5	2.68%	1.8%
p+Al, S	1.5-5	1.33%	2.9%
p+Al, N	2.5-5.5	2.83%	3.7%
p+Al, S	2.5-5.5	1.45%	5.8%
p+Au, N	2-5 (nominal)	2.38%	N/A
p+Au, S	2-5 (nominal)	1.16%	N/A
p+Au, N	1.5-5	2.37%	0.4%
p+Au, S	1.5-5	1.08%	6.9%
p+Au, N	2.5-5.5	2.39%	0.4%
p+Au, S	2.5-5.5	1.24%	6.9%
^{3}He+Al, N	2-5 (nominal)	2.24%	N/A
^{3}He+Al, S	2-5 (nominal)	1.59%	N/A
^{3}He+Al, N	1.5-5	2.19%	2.2%
^{3}He+Al, S	1.5-5	1.47%	7.5%
^{3}He+Al, N	2.5-5.5	2.35%	4.9%
^{3}He+Al, S	2.5-5.5	1.59%	0%

Table 7: Summary of changes in the ratio of $\psi(2s)/\psi(1s)$ when adjusting the range over which the mixed event background is normalized.

7 Results

Tab. 13 shows the ratios and uncertainties extracted for each of the data sets.

For all $p+p$ data, the North and South arms are averaged together following the procedure the PDG uses for combining different measurements of the same quantity. This gives a value of 2.43±0.18(stat) ±0.29(sys) for the ratio of inclusive $\psi(2s)/\psi(1s)$ in $p+p$. The statistical and systematic uncertainties are combined in quadrature and the data is plotted along with world data in Fig. 39

The same procedure is done bin-by-bin for the p_T dependent ratio. The results are shown in Fig. 40.

The p_T integrated double ratio is shown in Fig. 41. The error bars (boxes) on the points represent the statistical (systematic) uncertainties on the double ratio from the p+A data only. Since all the forward and backward rapidity points have a common $p+p$ reference, the uncertainties from this $p+p$ denominator are added in quadrature and quoted as the 14% global uncertainty in text on the plot. The midrapidity point is from PPG151.

Arm	Dimuon p_T model	Relative correction factor	Deviation from central value
N	m_T scaling (nominal)	0.806	N/A
S	m_T scaling (nominal)	0.836	N/A
N	forward R_{dA} modulation	0.796	1.2%
S	forward R_{dA} modulation	0.822	1.7%
N	backward R_{dA} modulation	0.801	0.6%
S	backward R_{dA} modulation	0.821	1.8%

Table 8: Summary of changes in the acc×eff correction to the $\psi(2s)/\psi(1s)$ when changing the simulation input parameters. A systematic uncertainty of 2% was assigned to each arm to cover this effect.

Uncertainty Source	North arm	South arm
$\psi(2s)$ width constraint	2.4%	3.5%
Second Gaussian width constraint	8.3%	13.2%
Mixed event mass range normalization	1%	1%
Relative acc×eff correction	2%	2%
Relative trigger efficiency	1%	1%
TOTAL	9%	13.9%

Table 9: Summary of systematic uncertainties on the $\psi(2s)/\psi(1s)$ ratio from the $p + p$ data.

Uncertainty Source	North arm	South arm
$\psi(2s)$ width constraint	2.9%	3.7%
Second Gaussian width constraint	1.3%	10.2%
Mixed event mass range normalization	2.8%	4.4%
Relative acc×eff correction	2%	2%
Relative trigger efficiency	1%	1%
TOTAL	4.8%	11.9%

Table 10: Summary of systematic uncertainties on the $\psi(2s)/\psi(1s)$ ratio from the p+Al data.

Uncertainty Source	North arm	South arm
$\psi(2s)$ width constraint	2.5%	3.5%
Second Gaussian width constraint	12.2%	12.1%
Mixed event mass range normalization	1%	6.9%
Relative acc×eff correction	2%	2%
Relative trigger efficiency	1%	1%
TOTAL	12.7%	14.5%

Table 11: Summary of systematic uncertainties on the $\psi(2s)/\psi(1s)$ ratio from the p+Au data.

Uncertainty Source	North arm	South arm
$\psi(2s)$ width constraint	2.5%	3.5%
Second Gaussian width constraint	13.6%	37.4%
Mixed event mass range normalization	3.6%	3.8%
Relative acc×eff correction	2%	2%
Relative trigger efficiency	1%	1%
TOTAL	14.4%	37.8%

Table 12: Summary of systematic uncertainties on the $\psi(2s)/\psi(1s)$ ratio from the He+Al data.

System	Arm	p_T range (GeV/c)	$\psi(2s)/\psi(1s)$ ratio (%)	Stat uncertainty	Sys uncertainty
$p+p$	combined	> 0	2.43	0.18	0.29
$p+p$	combined	0-1	1.51	0.25	0.18
$p+p$	combined	1-2	2.40	0.25	0.46
$p+p$	combined	2-3	3.83	0.51	0.29
$p+p$	combined	3-4	3.84	0.82	0.46
$p+p$	combined	4-6	3.72	1.38	0.46
p+Al	N	> 0	2.73	0.64	0.13
p+Al	S	> 0	1.37	0.61	0.16
p+Au	N	> 0	2.38	0.37	0.30
p+Au	S	> 0	1.16	0.42	0.17
^3He+Au	N	> 0	2.24	0.78	0.32
^3He+Au	S	> 0	1.59	0.67	0.60

Table 13: Summary of the measured $\psi(2s)/\psi(1s)$ ratios.

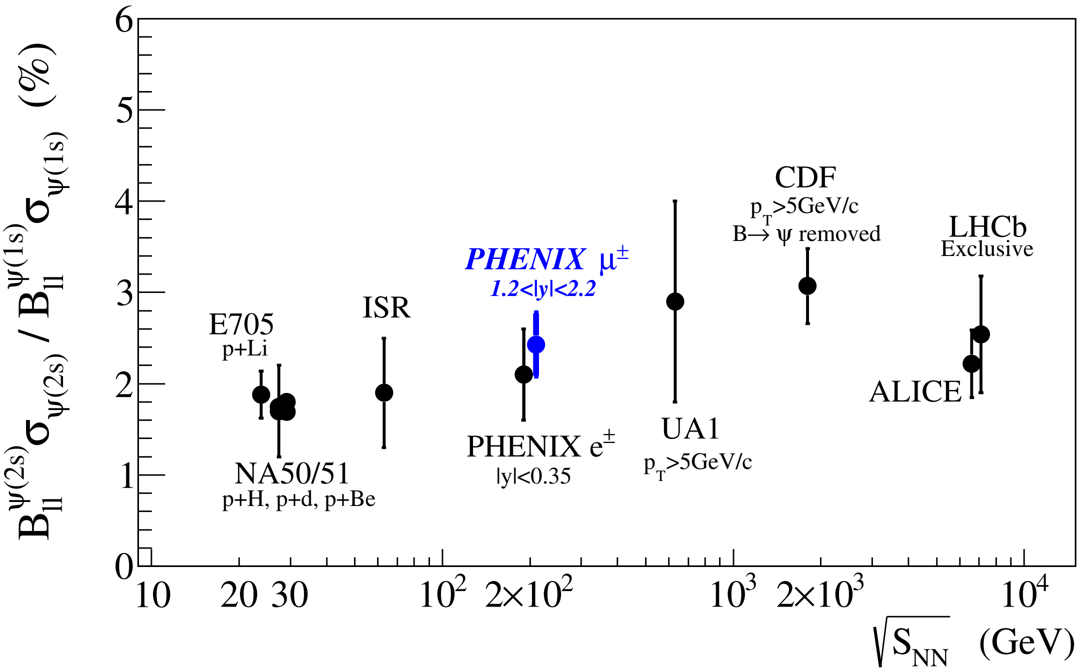

Figure 39: The combined N and S ratio for the $p+p$ data, compared to world data.

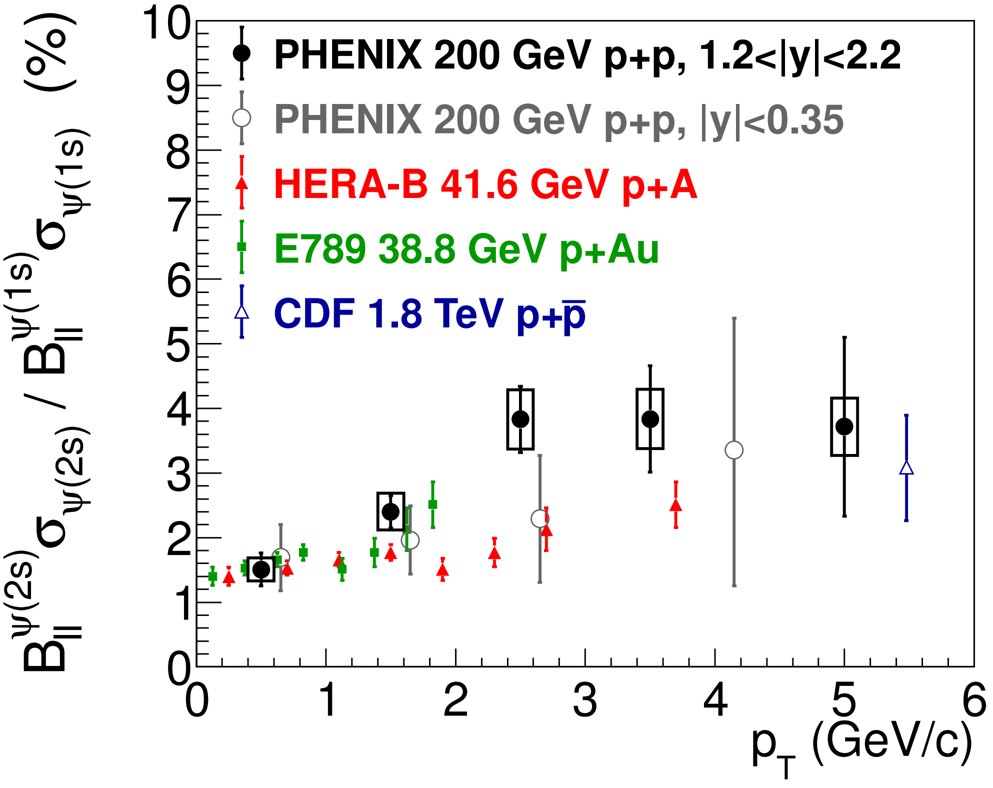

Figure 40: The combined N and S ratio for the $p + p$ data as a function of p_T, along with world data.

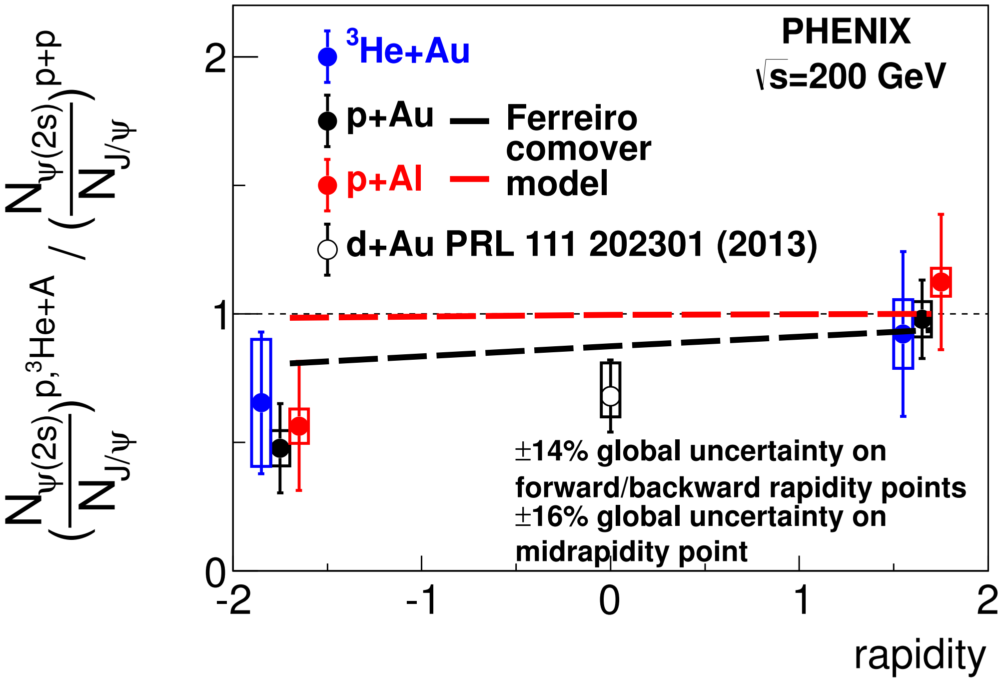

Figure 41: The double ratio, shown along with the central arm data point from PPG151.